



**HAL**  
open science

## UVIT view of NGC 5291: Ongoing star formation in tidal dwarf galaxies at 0.35 kpc resolution

R. Rakhi, Geethika Santhosh, Prajwel Joseph, Koshy George, Smitha Subramanian, Indulekha Kavila, J. Postma, Pierre-Alain Duc, Patrick Côté, Luca Cortese, et al.

### ► To cite this version:

R. Rakhi, Geethika Santhosh, Prajwel Joseph, Koshy George, Smitha Subramanian, et al.. UVIT view of NGC 5291: Ongoing star formation in tidal dwarf galaxies at 0.35 kpc resolution. Monthly Notices of the Royal Astronomical Society, 2023, 10.1093/mnras/stad970 . insu-04065896

**HAL Id: insu-04065896**

**<https://insu.hal.science/insu-04065896>**

Submitted on 12 Jul 2023

**HAL** is a multi-disciplinary open access archive for the deposit and dissemination of scientific research documents, whether they are published or not. The documents may come from teaching and research institutions in France or abroad, or from public or private research centers.

L'archive ouverte pluridisciplinaire **HAL**, est destinée au dépôt et à la diffusion de documents scientifiques de niveau recherche, publiés ou non, émanant des établissements d'enseignement et de recherche français ou étrangers, des laboratoires publics ou privés.

# UVIT view of NGC 5291: Ongoing star formation in tidal dwarf galaxies at $\sim 0.35$ kpc resolution

R. Rakhi,<sup>1</sup>★ Geethika Santhosh,<sup>1</sup> Prajwel Joseph,<sup>2,3</sup> Koshy George<sup>1</sup>,<sup>4</sup>★ Smitha Subramanian,<sup>2</sup> Indulekha Kavila,<sup>5</sup> J. Postma,<sup>6</sup> Pierre-Alain Duc,<sup>7</sup> Patrick Côté,<sup>8</sup> Luca Cortese<sup>1</sup>,<sup>9</sup> S. K. Ghosh,<sup>10</sup> Annapurni Subramaniam,<sup>2</sup> Shyam Tandon,<sup>11</sup> John Hutchings,<sup>8</sup> P. Samuel Wesley,<sup>3</sup> Aditya Bharadwaj<sup>3</sup> and Neeran Niroula<sup>3</sup>

<sup>1</sup>Department of Physics, NSS College, Pandalam, Kerala 689 501, India

<sup>2</sup>Indian Institute of Astrophysics, Bangalore 560034, India

<sup>3</sup>Department of Physics and Electronics, CHRIST (Deemed to be University), Bangalore 560029, India

<sup>4</sup>Faculty of Physics, Ludwig-Maximilians-Universität, Scheinerstr. 1, D-81679 Munich, Germany

<sup>5</sup>School of Pure and Applied Physics, Mahatma Gandhi University, Kottayam, Kerala 686560, India

<sup>6</sup>Department of Physics and Astronomy, University of Calgary, 2500 University Drive NW, Calgary, Alberta T2N 1N4, Canada

<sup>7</sup>Université de Strasbourg, CNRS, Observatoire astronomique de Strasbourg, UMR 7550, F-67000 Strasbourg, France

<sup>8</sup>Herzberg Astronomy and Astrophysics Research Centre, National Research Council of Canada, 5071 W. Saanich Road, Victoria, BC V9E 2E7, Canada

<sup>9</sup>International Centre for Radio Astronomy Research (ICRAR), University of Western Australia, Crawley, WA 6009, Australia

<sup>10</sup>Tata Institute of Fundamental Research, Colaba, Mumbai 400005, India

<sup>11</sup>Inter-University Centre for Astronomy and Astrophysics, PostBag 4, Ganeshkhind, Pune 411007, India

Accepted 2023 March 27. Received 2023 March 14; in original form 2023 January 10

## ABSTRACT

NGC 5291, an early-type galaxy surrounded by a giant HI ring, is believed to be formed from collision with another galaxy. Several star forming complexes and tidal dwarf galaxies are distributed along the collisional ring which are sites of star formation in environments where extreme dynamical effects are involved. Dynamical effects can affect the star formation properties and the spatial distribution of star forming complexes along the tidal features. To study and quantify the star formation activity in the main body and in the ring structure of the NGC 5291 system, we use high spatial resolution FUV and NUV imaging observations from the Ultraviolet Imaging Telescope onboard AstroSat. A total of 57 star-forming knots are identified to be part of this interacting system out of which 12 are new detections (star forming complexes that lie inside the HI contour) compared to the previous measurements from lower resolution UV imaging. We estimate the attenuation in UV for each of the resolved star-forming knots using the UV spectral slope  $\beta$ , derived from the FUV – NUV colour. Using the extinction corrected UV fluxes, we derive the star formation rate of the resolved star forming complexes. The extinction corrected total star formation rate of this system is estimated as  $1.75 \pm 0.04 M_{\odot} \text{ yr}^{-1}$ . The comparison with dwarf galaxy populations (BCD, Sm, and dIm galaxies) in the nearby Universe shows that many of the knots in the NGC 5291 system have SFR values comparable to the SFR of BCD galaxies.

**Key words:** stars: formation – galaxies: dwarf – galaxies: formation – galaxies: interactions – galaxies: star formation – ultraviolet: galaxies.

## 1 INTRODUCTION

Study of galaxy mergers and interactions are of great importance in advancing our current understanding of galaxy formation and evolution (Conselice et al. 2003; Pearson et al. 2019). In the hierarchical  $\Lambda$  Cold Dark Matter ( $\Lambda$ CDM) clustering paradigm, large massive haloes form and grow by the merging or clustering of low mass haloes. The hierarchical clustering model predicts that massive galaxies must have undergone several merging activities in the past. This leads to the possibility of dwarf galaxies being the

primary ingredients in the formation of the large galaxies we see in the nearby universe (White & Rees 1978; White & Frenk 1991).

The local Universe is observed to have several interacting or merging galaxy systems characterized by dust and gas-rich tidal tails, collisional rings, and tidal bridges (Buta & Crocker 1993; Higdon 1995; Sotnikova & Reshetnikov 1998). Tidal dwarf galaxies (TDGs) are gravitationally bound systems of gas and stars formed during interaction of galaxies and are kinematically decoupled from the surrounding tidal debris. During close encounters between gas-rich galaxies, neutral hydrogen gas (HI), stars and dust from the discs of the galaxies can get pulled out by tidal forces/gravitational torques (Bournaud 2010) forming rings, tidal tails, bridges, and plumes. Star formation takes place in the gas thrown out of the galaxies during tidal interactions. Star forming knots or clumps are observed along

\* E-mail: [rakhi@nsscollegepandalam.ac.in](mailto:rakhi@nsscollegepandalam.ac.in) (RR); [koshyastro@gmail.com](mailto:koshyastro@gmail.com) (KG)

the tidal features (Struck 1999) and the massive clumps are potential young TDG candidates (Mirabel, Dottori & Lutz 1992; Elmegreen, Kaufman & Thomasson 1993; Alonso-Herrero et al. 2000; Duc, Bournaud & Masset 2004; Hancock et al. 2009; Duc 2012). The most massive TDGs in an interacting system may evolve to become self-bound dwarf galaxies that may detach from the host system (Duc & Mirabel 1999). Once separated from their progenitors, they will closely resemble the independent dwarf galaxy populations. Being pre-enriched these TDGs are more metal rich than isolated dwarf galaxies of the same luminosity. This property of TDGs can be used to identify these recycled dwarf galaxies and to investigate the origin of their building material in the disc of their progenitors (Hunter, Hunsberger & Roye 2000).

TDGs comprise of young stars, which are formed from the recent collapse of ejected H I clouds as well as the older stellar population coming from the disc of their parent galaxies. Duc & Mirabel (1999) studied the relative proportion of both these populations using multiwavelength observations of several interacting systems in the nearby Universe. They proposed that TDGs are divided into two categories. Category 1 consists of extremely young objects, forming their first generation of stars (e.g. dwarfs around NGC 5291). These have high star formation rates (SFR) similar to that of blue compact dwarf (BCD) galaxies. Category 2 corresponds to galaxies dominated by the older stellar population coming from the disc of their progenitors and these galaxies resemble dwarf irregulars (e.g. NGC 2992) (Duc et al. 2000; Bournaud 2010).

Young, hot, massive, and luminous O, B, A stars on the main sequence give out immense amount of ultraviolet (UV) radiation and therefore regions of ongoing star formation could appear bright in ultraviolet images. The ultraviolet continuum is thus a direct tracer of recent star formation in galaxies ( $\sim 200$  Myr) (Kennicutt & Evans 2012). With the advent of UV missions capable of providing deep and high resolution UV images of extragalactic systems, a quantitative analysis of the star formation activity in star forming knots in terms of the SFR is possible. Tidal dwarf galaxy formation is connected to merging or interacting galaxies in the universe (Okazaki & Taniguchi 2000). TDGs with ongoing star formation are important structures to study the process of star formation in the smallest mass systems (dwarf galaxies) also. NGC 5291 is an interacting galaxy system that lies in the western outskirts of the cluster Abell 3574. The system comprises of an early-type galaxy NGC 5291 (morphological type: SA.0+) and a companion galaxy called ‘the Seashell’ (morphology: distorted edge-on spiral) interacting with it (Longmore et al. 1979).

The system has extensions or tails, defined by knots, emerging from the galaxy. Deep optical and spectroscopic studies of NGC 5291 pointed out that the optical knots that extend to the north and south of the system may be sites of recent star formation (Pedersen, Gammelgaard & Laustsen 1978; Longmore et al. 1979). 21 cm radio observations, using the Very Large Array (VLA), revealed a giant collisional H I ring structure connected to the NGC 5291 system which indicated that the knots observed are indeed star forming complexes that may even be young tidal dwarf galaxies (Malphrus et al. 1997; Bournaud et al. 2007). The fragmented H I ring structure, which hosts numerous intergalactic H II regions of the NGC 5291 system, is exceptional in itself because of its moderately high metallicity ( $8.4 \leq 12 + \log(O/H) \leq 8.6$ ) and the absence of an old stellar population. This suggests that the dwarf galaxies observed in the system are in fact young tidal dwarf galaxies formed from the pre-enriched gas in the collisional/tidal debris (Duc & Mirabel 1998).

Many studies of the NGC 5291 system in the ultraviolet have come up over the past few decades consequent to observations using the *Far Ultraviolet Space Telescope (FAUST)* (Bixler et al. 1984), the

*Hubble Space Telescope (HST)*, and the *Galaxy Evolution Explorer (GALEX)* (Deharveng et al. 1994; Boquien et al. 2007, 2009; Fensch et al. 2019; Elmegreen et al. 2020). Among these, *GALEX* is fully dedicated to observations in the ultraviolet regime and is capable of providing wide field ( $1.2^\circ$ ) far ultraviolet (FUV) and near ultraviolet (NUV) images with a spatial resolution of 4.2 arcsec/5.3 arcsec (FUV/NUV) (Morrissey et al. 2007). Boquien et al. (2007) presented a polychromatic view of NGC 5291 based on *GALEX* observations together with archival H  $\alpha$ , 8  $\mu\text{m}$ , and H I data. They identified 29 star forming regions along the ring structure and determined their SFR. More recently, Fensch et al. (2019), using *HST* data, studied massive star cluster formation in the three TDGs (NGC 5291N, NGC 5291S, and NGC 5291 SW) associated with the NGC 5291 system.

In this paper, we present high resolution ultraviolet imaging observations (in Far and Near UV bands, FUV: 1.4 arcsec and NUV: 1.2 arcsec) of the NGC 5291 system using data from the Ultraviolet Imaging Telescope (UVIT) on board *AstroSat*. The main aim of the paper is to identify and characterize the star forming knots in the tidal tails and determine the star formation rates in these knots at the best possible resolution, taking into account dust attenuation of the ultraviolet spectrum. This paper is outlined as follows. Section 2 of the paper describes data acquisition, data reduction, source extraction, and identification in detail. The results are discussed in Section 3 and conclusions are presented in Section 4.

Throughout the paper, magnitudes are computed in AB system (Oke & Gunn 1983). The value of the Hubble parameter  $H_0$  used is  $72 \text{ km s}^{-1} \text{ Mpc}^{-1}$ , assuming flat  $\Lambda$ CDM cosmology. For this value of  $H_0$ , the distance (D) to NGC 5291 is 62 Mpc (Boquien et al. 2007) and 1 arcsec in the sky corresponds to 0.296 kpc at system rest frame.

## 2 DATA AND ANALYSIS

NGC 5291 (RA:206.852,Dec:−30.407)<sup>1</sup> has been observed (PI: K. George, proposal ID: G07.003) with Ultraviolet Imaging Telescope (UVIT) on board *AstroSat* (Kumar et al. 2012). UVIT performs imaging simultaneously in three channels: visible (320–550 nm), the near-ultraviolet (NUV: 200–300 nm), and the far-ultraviolet (FUV: 130–180 nm). UVIT has a set of filters mounted on a wheel to facilitate imaging in the NUV and FUV in different narrow and broad wavelength bands. The field of view of UVIT is 28 arcmin in diameter. UVIT has a resolution of  $\sim 1.4$  arcsec in FUV and  $\sim 1.2$  arcsec in NUV. This implies that UVIT can resolve star forming knots in NGC 5291 down to approximately 0.35 kpc at NUV and 0.41 kpc at FUV.

### 2.1 Data

We use Level 1 (L1) UVIT data of NGC 5291. For the multiple orbit observations of the target field NGC 5291, the filters used are NUV: N242W and FUV: F148W. Details on the UVIT filter combinations and the performance parameters for the individual filters are given in Tandon et al. (2017). We have reported the filter details and the integration time of the UVIT observations of NGC 5291 in Table 1. A H I map of the galaxy, obtained with the VLA (Bournaud et al. 2007) is used for identifying the relevant star-forming knots. To check whether the detections are bona fide knots, we use the observations

<sup>1</sup><https://ned.ipac.caltech.edu/>

**Table 1.** NGC 5291 UVIT observations.

Channel	Filter name	$\lambda_{\text{mean}}$ (Å)	$\Delta\lambda$ (Å)	Integration time (s)
FUV	F148W	1481	500	8242
NUV	N242W	2418	785	8079

from the Dark Energy Camera Legacy Survey (DECaLS) DR10 imaging data in three optical filters ( $g, r, z$ ) (Dey et al. 2019).<sup>2</sup>

## 2.2 Data reduction

L1 data of NGC 5291 is reduced to Level 2 (L2) scientific images using CCDLAB (Postma & Leahy 2017, 2021). Using CCDLAB, UVIT data are corrected for fixed pattern noise, distortion and drift, and flat fielded. The orbit-wise images are aligned to a common frame before merging the data. The PSF of master NUV and FUV images are optimized. Finally, the images are aligned with respect to the sky coordinates using the automated WCS solver in CCDLAB (Postma & Leahy 2020). The NUV and FUV images have  $4096 \times 4096$  pixel array size where one pixel corresponds to 0.416 arcsec.

The NUV and FUV images thus created are used for further analysis. Flux calibration is done for NUV and FUV images using the zero point and unit conversion factors given in Tandon et al. (2017) and updated in Tandon et al. (2020).

## 3 NGC 5291 UV IMAGING

Fig. 1 shows the false-colour combined image of the NGC 5291 system created from the UVIT FUV and NUV images (North is up and East is towards the left of the image) overlaid with Legacy survey  $z$  band image. Here, FUV is given in blue, NUV in green, and DECaLS  $z$  band image is given in red. The interacting galaxies NGC 5291 and the Seashell are located towards the centre of the image. As seen in Fig. 1, several UV bright knots extend towards the north, south, and south-west directions following the fragmented ring structure seen in H I imaging data.

### 3.1 Source extraction

The sources from the FUV and NUV images are extracted using the photometry package ProFound (Robotham et al. 2018). ProFound is capable of both source identification and photometric extraction. It detects sources in noisy images, then generates segmentation maps by identifying the pixels belonging to each source, and measures statistics including flux, size, and ellipticity. ProFound first detects pixels from the intensity map that are above a threshold value and these pixels are allowed to grow or dilate freely until a certain intensity limit is reached based on the set threshold. The dynamic dilation will ensure close to total magnitudes regardless of the differing PSFs. ProFound uses watershed algorithm for de-blending pixels that are above the threshold value. The deblended collection of pixels that are above a threshold is called a segment. This method of segmentation is unique as it does not assume a fixed aperture for an object and the segment corresponding to a source agrees with the underlying morphology of the source. After segmentation, ProFound extracts the image data flux from each of the pixels that are part of the segments.

ProFound was run on the slightly lower resolution FUV image. Along with the FUV image, the sky and sky RMS values were given as inputs to the ProFound function and it extracted 206 sources along with their flux, magnitude, and area for sources from the entire UVIT field of view. For NUV source extraction, we provided the dilated FUV segmentation map created by ProFound as an additional input to the function to make sure that the same source position is used for both NUV and FUV.

The segmentation map obtained from ProFound, overlaid by H I contour, showing the extend of each UV source is given in Fig. 2. ProFound assigns a unique number called the segID for each segment of the map. Different colours in Fig. 2 corresponds to different segIDs. The circled regions correspond to the galaxies, NGC 5291 and Seashell.

### 3.2 Identification of star-forming knots

In order to identify the star-forming knots that are part of the NGC 5291 interacting system, we analysed the FUV–NUV colour distribution of all the sources in the UVIT field of view with a signal-to-noise ratio (SNR) greater than 5. The Gaussian fitted histogram of the UV colour (FUV–NUV) of these sources is shown in Fig. 3. The mean ( $\mu$ ), standard deviation ( $\sigma$ ), and full width at half-maximum (FWHM) of the best fit are 0.26 mag, 0.39 mag, and 0.93 mag, respectively. From this, we consider those 109 sources that lie within a  $1\sigma$  colour range, for further analysis. Due to the lack of redshift information for the knots, the sources that are part of the system are identified based on location within the H I contour.

#### 3.2.1 Sources lying within the H I contour

All the knots that fall within the H I contour are identified with the help of SAOImageDS9 (Joye & Mandel 2003). Out of the 109 sources that lie within  $1\sigma$  colour range, 64 sources lie inside the H I column density contour and 45 sources lie outside (Fig. 2).

#### 3.2.2 Sources lying outside the H I contour

Among the 45 sources that lie outside the H I contour, some lie far away from the NGC 5291 interacting system. Hence we consider only those knots which are lying nearer to the H I contour for further analysis. For this, we consider the sources that are lying within a circle, which is centred at the NGC 5291-central galaxy and has a radius roughly half the diameter of the projected H I ring. We find that a total of 10 sources out of 45 lie within this region.

In order to confirm that the selected sources (both inside as well as outside the H I contour) are star-forming regions and to check for any possible contamination, we make a comparison of these knots with DECaLS image of the system. The star-forming knots appear blue in the DECaLS image and other knots seem to be contaminated by foreground/background sources. Thus we further eliminate a total of 17 sources (10 inside the H I contour and 7 outside the H I contour) which are possibly foreground/background sources.<sup>3</sup> We finally have a total of 57 star-forming (SF) knots (54 inside the H I contour and 3 outside the H I contour) for this study.

Fig. 4 depicts the distribution of UV clump sizes for the resolved knots. The selected star forming knots of the NGC 5291 system (using FUV) are shown Fig. 5.

<sup>2</sup><https://www.legacysurvey.org/viewer>

<sup>3</sup>The list of possible contaminant sources are given in the appendix.

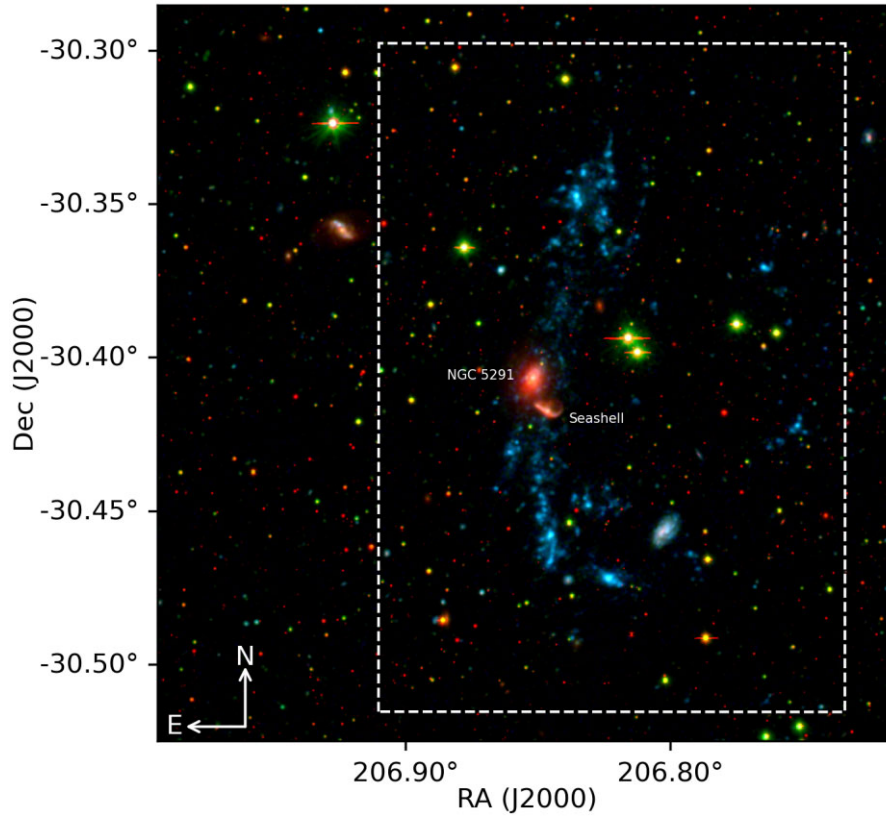


**Figure 1.** Colour composite image of the NGC 5291 system made using FUV (blue), NUV (green), and DECaLS  $z$  band image (red). The dashed rectangle shows the region of interest. (Field of View: 21.8 arcmin  $\times$  11.6 arcmin).

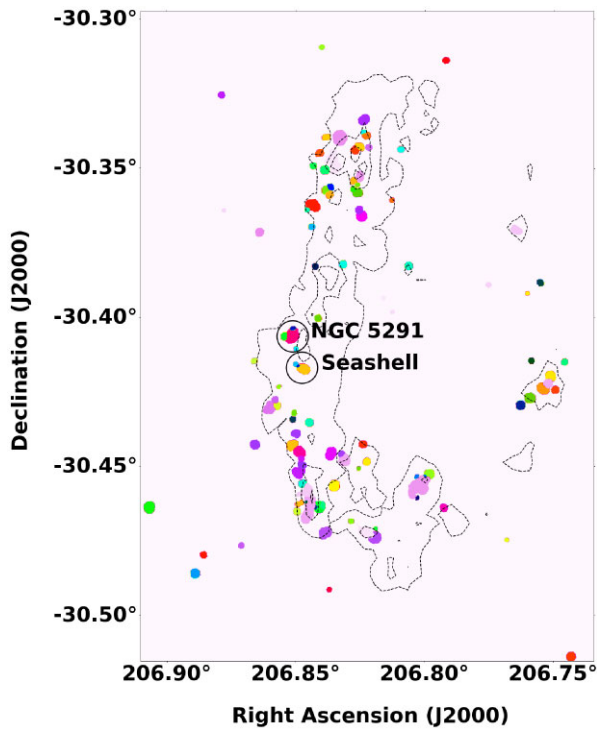


**Figure 2.** Segmentation map from ProFound overlaid by H I contour. The circled regions correspond to the galaxies, NGC 5291 and Seashell.

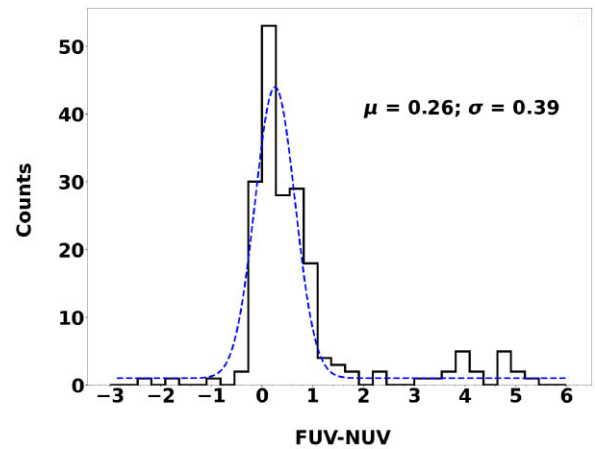


**Figure 3.** Distribution of FUV–NUV colour of all the sources above  $5\sigma$  detection threshold in both FUV and NUV.

## 4 RESULTS

### 4.1 Comparison with previous UV observations

We first compare our high resolution UV image with the results from the earlier UV mission *GALEX*, which has a resolution  $\sim 4$ – $5$  arcsec. The 54 star forming regions of the NGC 5291 system that lie inside the H I contour obtained with UVIT have been compared against *GALEX*. The study of the NGC 5291 system using *GALEX* reported 29 knots within the same region (Boquien et al. 2007, 2009).

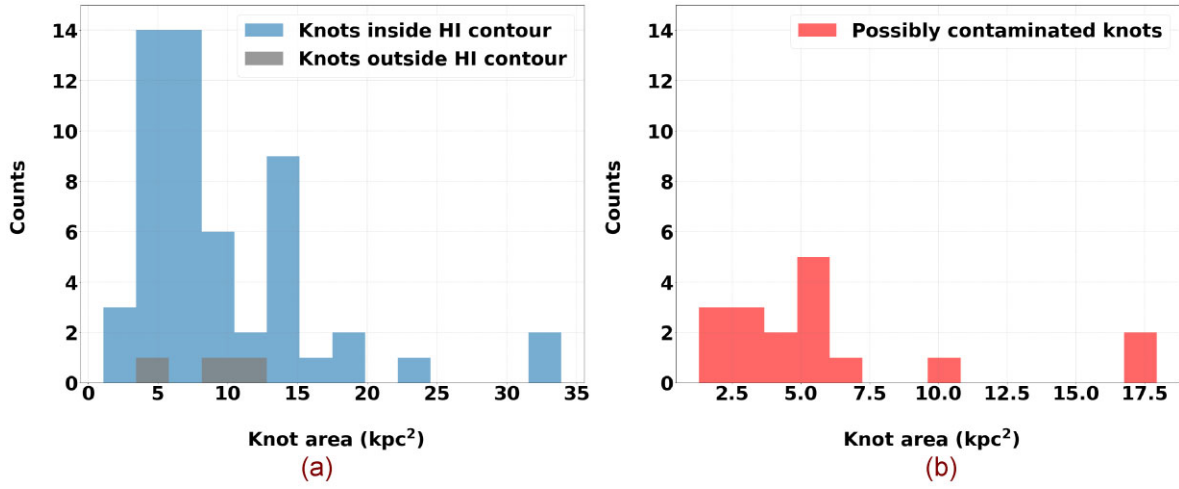


**Figure 4.** Distribution of areas (in  $\text{kpc}^2$ ) of the resolved knots: (a) Uncontaminated regions; (b) Possibly contaminated regions.

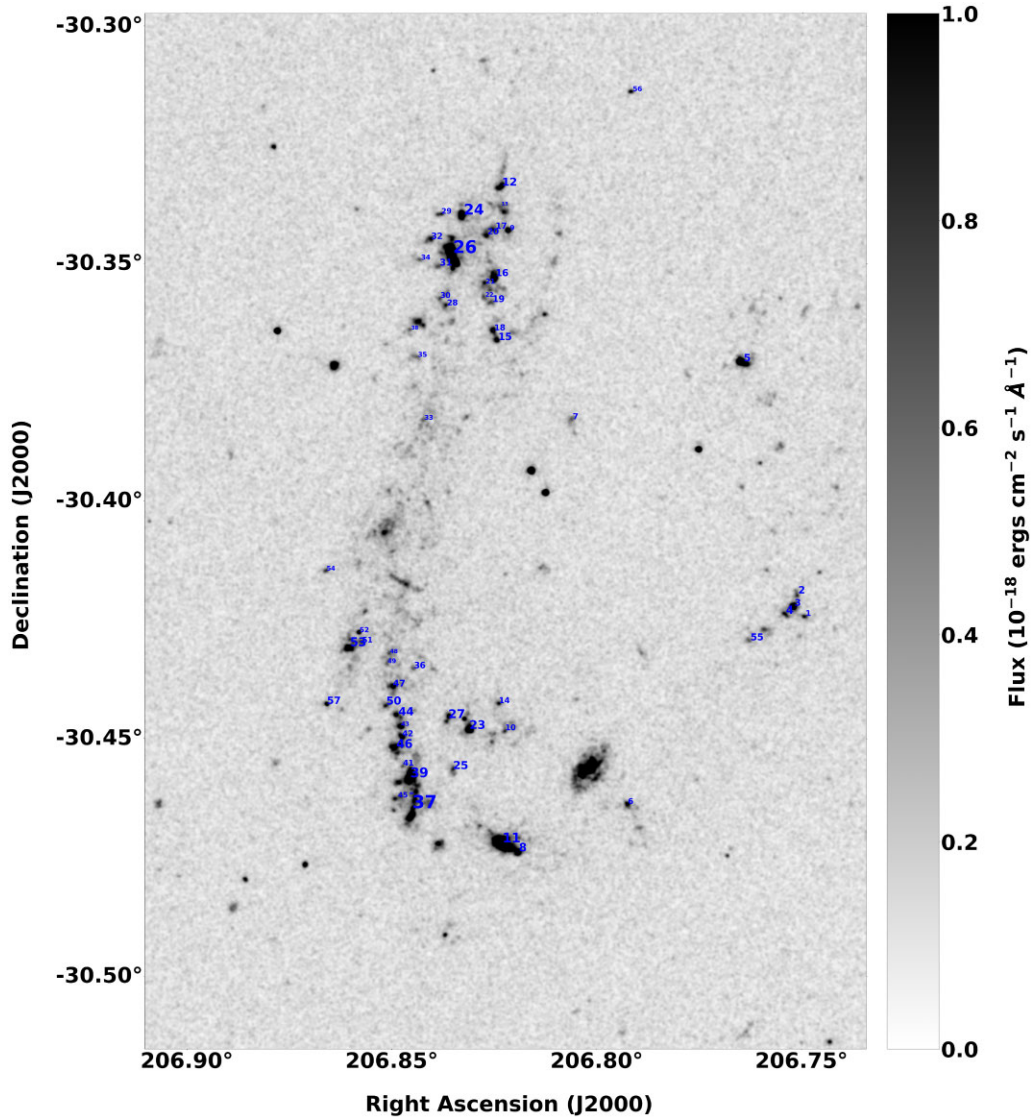


**Figure 5.** Selected star forming knots of the NGC 5291 system marked on FUV image. The individual knots are labelled using numbers, and the sizes of these labels represent the relative sizes of the knots. Annotated regions 1 to 57 are the knots.

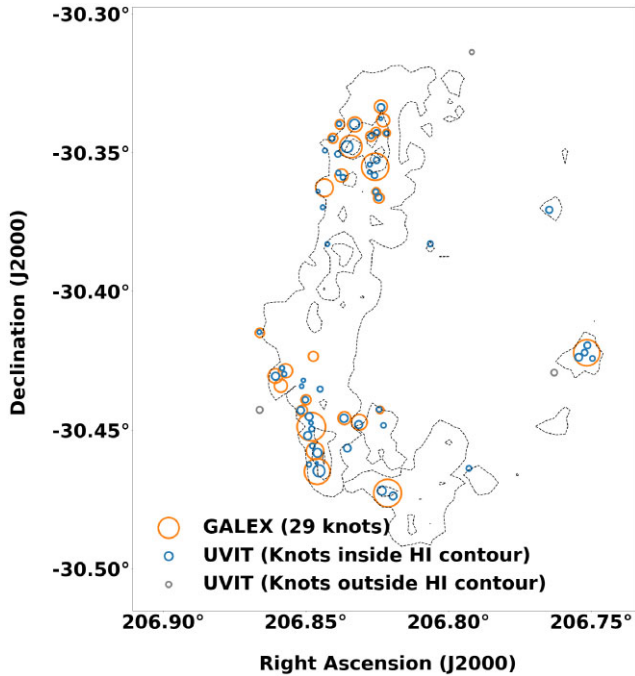


**Figure 6.** Knots in the *GALEX* study (Boquien et al. 2007, 2009) overlaid on the scatter plot of selected knots in this study. The sizes of the markers for the knots represent their relative sizes.

A comparison of the selected knots in this study to the knots in the *GALEX* study is shown in Fig. 6. We note that 12 of the 54 UVIT knots selected within the H I contour are unreported in the *GALEX*-based study. It is further observed that several of the knots which appeared as a single entity in the *GALEX* images are well resolved by UVIT into two or more knots (see Fig. 7).

Fig. 8 shows the distributions of fluxes (uncorrected for extinction) for the knots in UVIT and *GALEX* (Boquien et al. 2009).

It is seen that the flux distribution for the knots in UVIT has moved to the low flux values as compared to *GALEX*. This can be attributed to the improved spatial resolution of UVIT in comparison with *GALEX* which enabled better deblending of structures.

#### 4.2 Slope of the UV continuum $\beta$ and extinction $A_{FUV}$

The interstellar medium within the star forming knots can contain significant amount of dust. The UV radiation emitted by young massive O,B,A stars can get attenuated by dust. Dust grains can scatter and absorb UV radiation and this can greatly complicate the interpretation of the detected UV emission. Determining the level of dust attenuation is crucial in accurately deriving intrinsic UV luminosity and hence star formation rates. The slope of ultraviolet continuum has been proposed as a powerful diagnostic of dust attenuation in star-forming galaxies (Overzier et al. 2011; Boquien et al. 2012). The UV continuum spectrum of star forming galaxies is characterized by the spectral index  $\beta$  where  $f_\lambda \propto \lambda^\beta$  (Calzetti, Kinney & Storchi-Bergmann 1994) for  $\lambda > 1200 \text{ \AA}$ ,  $f_\lambda$  ( $\text{erg cm}^{-2} \text{ s}^{-1} \text{ \AA}^{-1}$ ) is the flux density of the source. For the case of UVIT FUV and NUV passbands,

$$\beta_{\text{-UVIT}} = 1.88(m_{\text{FUV}} - m_{\text{NUV}}) - 2.0, \quad (1)$$

where  $m_{\text{FUV}}$  and  $m_{\text{NUV}}$  are the magnitudes in FUV and NUV, respectively.

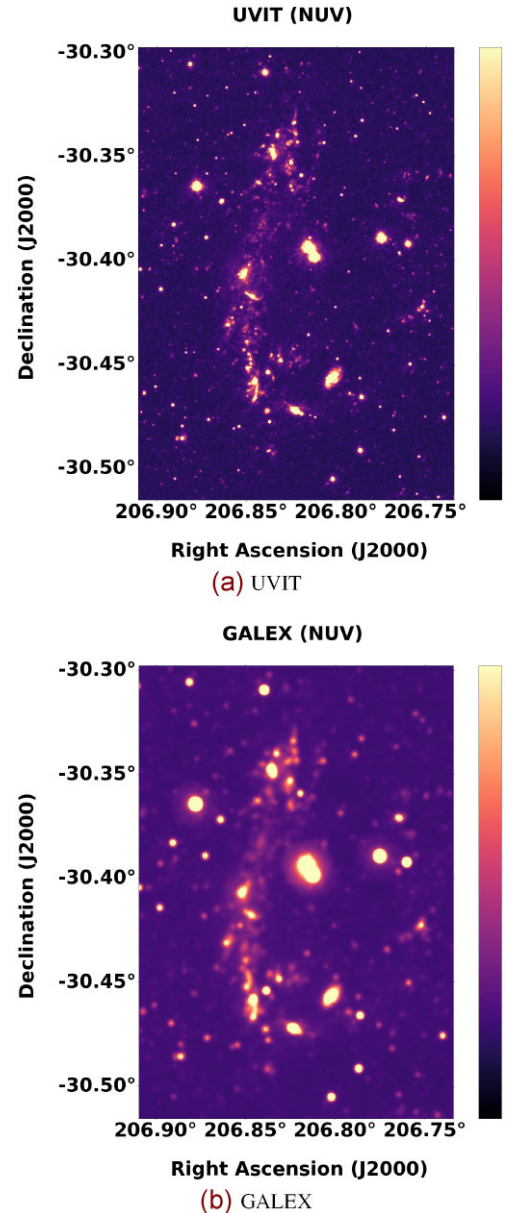


**Figure 7.** Comparison of NUV images for NGC 5291 taken with UVIT (top) and *GALEX* (bottom). North is up and east is to the left.

Meurer, Heckman & Calzetti (1999) (hereafter, M99) established a relationship between the UV spectral slope  $\beta$  and the ratio of far infrared (FIR) and UV fluxes for a sample of starburst galaxies. This method relates the FIR and UV radiation emitted from galaxies. It is considered to be a powerful tool in recovering the UV radiation lost due to the dust, regardless of the geometry of the dust.

We use the M99 relation for the starburst case to determine dust attenuation from  $\beta$  which is given as,

$$A_{\text{FUV}} = 4.43 + 1.99\beta, \quad (2)$$

where  $\beta$  is given by equation (1) for our case.

A histogram showing the slope of UV continuum  $\beta$  for the selected knots in the NGC 5291 system is presented in Fig. 9. The numerical value of  $\beta$  ranges from  $-2.18$  to  $-1.73$  (see Appendix for details).

Fig. 10 gives the spatial distribution of  $A_{\text{FUV}}$  for the selected knots and the value of  $A_{\text{FUV}}$  ranges from 0.05 to 0.99.

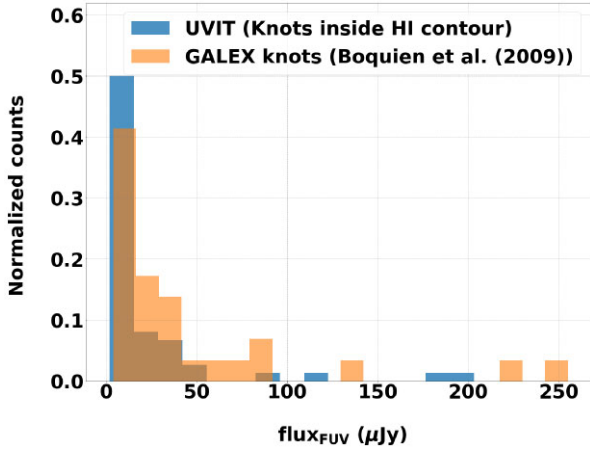


**Figure 8.** Comparison of the flux values for the knots measured from UVIT and *GALEX* FUV imaging data (Boquien et al. 2009).

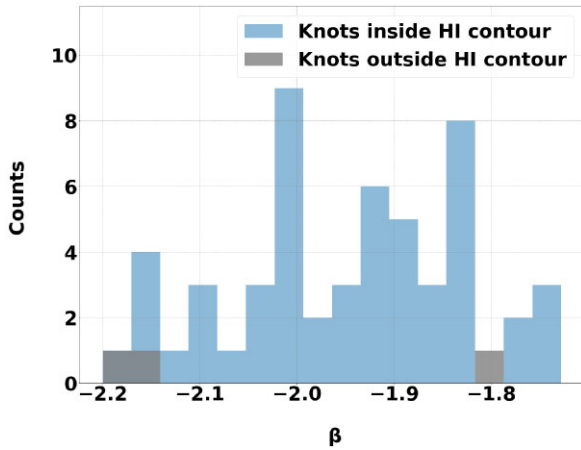


**Figure 9.** Histogram of the values of the slope of the UV continuum  $\beta$ .

### 4.3 Star formation rates of the knots

The measured FUV flux of the knots are corrected for extinction using the  $A_{FUV}$  values computed for each knot. Ultraviolet flux is a direct tracer of ongoing star formation and the star formation rate (SFR) can be calculated from the extinction corrected UV luminosity (Kennicutt & Evans 2012).

For the computation of the SFR, the following form of the relation is used which assumes a constant rate of star formation over a time-scale of  $10^8$  yr, with a Salpeter initial mass function (IMF) (Salpeter 1955) from 0.1 to  $100 M_{\odot}$  as described in Iglesias-Páramo et al. (2006) and in Cortese, Gavazzi & Boselli (2008)

$$\text{SFR}_{FUV} [M_{\odot} \text{ yr}^{-1}] = \frac{L_{FUV} [\text{erg s}^{-1}]}{3.83 \times 10^{33}} \times 10^{-9.51}, \quad (3)$$

where  $L_{FUV}$  is the extinction corrected FUV luminosity.

The total extinction corrected star formation rate, derived from the FUV flux, for the SF knots lying within the HI contour (excluding that of NGC 5291 and the Seashell galaxies) amounts to  $1.72 \pm 0.04 M_{\odot} \text{ yr}^{-1}$  and the same for the knots that lie outside HI contour is  $0.026 \pm 0.004 M_{\odot} \text{ yr}^{-1}$ . The SFR of the galaxies, NGC 5291 and the Seashell is  $1.93 \pm 0.21$  and  $1.16 \pm 0.16 M_{\odot} \text{ yr}^{-1}$ , respectively.

## 5 DISCUSSION

There exists many observational studies on the star formation and TDG formation in interacting systems in the UV using *GALEX* data (Hibbard et al. 2005; Neff et al. 2005; Boquien et al. 2009; Hancock et al. 2009; Sheen et al. 2009). Boquien et al. (2009) made a detailed multiwavelength (UV, infrared, and  $H\alpha$ ) analysis of six interacting systems with star forming regions. The interacting systems considered by them include NGC 5291, Arp 105, Arp 245, NGC 7252, Stephan’s Quintet (SQ), and VCC 2062. George et al. (2018) performed a detailed study using UVIT on star formation in TDGs along the tails of the post-merger system NGC 7252.

The main concern in the estimation of SFRs using UV flux is the effect of dust attenuation. Dust plays a significant role in the attenuation of UV flux in galaxies. A common technique for measuring the extinction towards stars in our Galaxy is to use the colour excess. If a star’s spectral type (and therefore its intrinsic colour) is known, the extinction towards it can be determined. However, this technique cannot be applied to galaxy systems, as the relative extinction at different wavelengths is sensitive to the unknown relative geometry of stars and dust, and differs for different optical depths (Trewella 1998).

The  $L_{IR}/L_{UV}$  ratio has been identified as one of the powerful estimators of dust attenuation in star-forming galaxies (e.g. Gordon et al. 2000; Buat et al. 2005). From UV and FIR (*Spitzer/Herschel*) data available for NGC 5291, one could directly measure the dust attenuation from FIR/UV, but not at the spatial resolution of UVIT. The relation established by Meurer et al. (1999) between the slope of the rest-frame UV continuum  $\beta$  and dust attenuation deduced from their  $L_{IR}/L_{UV} - \beta$  relation for local starburst galaxies is hence used to determine the extinction towards the knots.

In this paper, we have analysed the extinction in the star forming regions associated with the NGC 5291 interacting system using high resolution UVIT data. The SFR for the knots of the selected knots of the NGC 5291 system has been computed from corrected UV luminosities. The spatial distribution of extinction corrected FUV star formation rate ( $\text{SFR}_{FUV}$ ) of the selected knots in NGC 5291 interacting system is presented in Fig. 11. The extinction corrected SFR (log SFR) of the knots ranges from  $-2.80$  to  $-0.53$ . The M99 relation provides us with accurate estimates of the attenuation for starburst galaxies (Overzier et al. 2011; Boquien et al. 2012). Considering the ongoing star formation in the NGC 5291 system to be more like a starburst, the M99 relation is used here for the estimation of extinction. This is the first time such an analysis is performed on the NGC 5291 system. UVIT has resolved the star forming regions in comparison to the previous UV mission *GALEX*. Several of the knots that appeared as a single entity in the *GALEX* images have been resolved into two or more knots in the UVIT images. This enabled the estimation of the extinction to the smallest scales that have been ever possible for NGC 5291. The UVIT based extinction corrected SFRs for the selected knots in this study is compared with that of the previously measured SFR values given in Boquien et al. (2007) and shown in Fig. 12.

In order to check whether the recently formed TDGs exhibit SFR values comparable to other dwarf galaxies of similar stellar masses in the local universe, we compared the extinction corrected SFR values of the selected knots in the NGC 5291 system with the SFR values of dwarf galaxies (e.g. BCD), Sm and dIm galaxies in the local universe as determined using *GALEX* FUV data by Hunter, Elmegreen & Ludka (2010) as well as with the uncorrected SFR of knots in NGC 7252 system as given in George et al. (2018). Histograms for the SFR values of the aforementioned systems are shown in Fig. 13. We

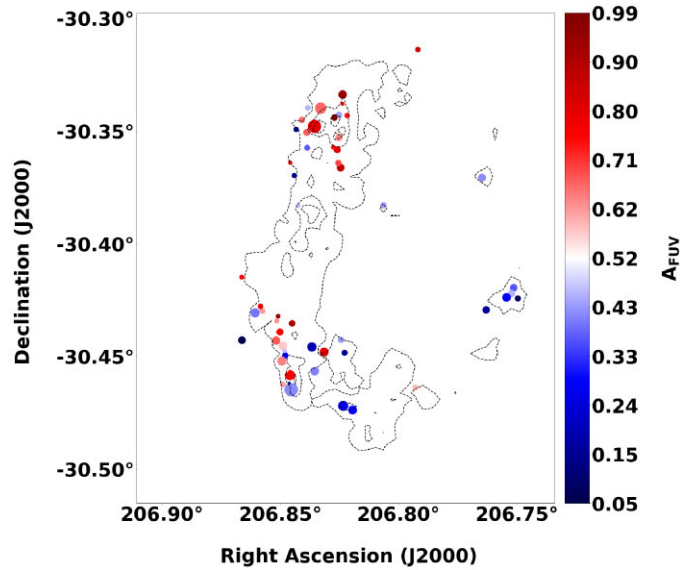


Figure 10. Spatial distribution of dust attenuation  $A_{FUV}$  of the selected knots in the NGC 5291 system.

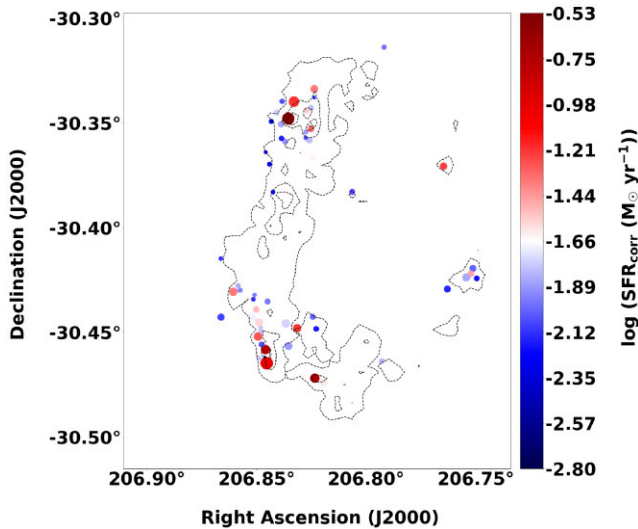


Figure 11. Spatial distribution of star formation rate  $SFR_{FUV}$  of the selected knots in the NGC 5291 system.

note that the values are very similar to the uncorrected SFR of star forming knots detected in NGC 7252 from UVIT imaging. From the histogram, it is further noted that  $\log$  SFRs of the selected knots in the NGC 5291 system is greater than  $-3$ . The distribution of SFRs in the knots is similar to those of dIm galaxies for  $\log$  SFR greater than  $-3$ . The maximum value of  $\log$  SFR is similar for the knots in the NGC 5291 system, dIm and BCD galaxies. It is also seen that many of the knots associated with the NGC 5291 system have high SFRs similar to BCD galaxies; this is characteristic of Category 1 TDGs. The three known tidal dwarf galaxies in the system, located to the north – NGC 5291N, south – NGC 5291S (Duc & Mirabel 1998, 1999; Higdon, Higdon & Marshall 2006) and south-west – NGC 5291SW have SFR values of 0.30, 0.30, and  $0.22 M_{\odot} \text{ yr}^{-1}$ , respectively. They are located far from the centre of the system and are located at peaks in the HI column density map. The highest  $\log$  SFR values reported by Hunter et al. (2010) for dIm, BCD and Sm galaxies in their samples are  $-0.62$ ,  $-0.62$ , and  $-0.94$ , respectively, while the  $\log$  SFR of

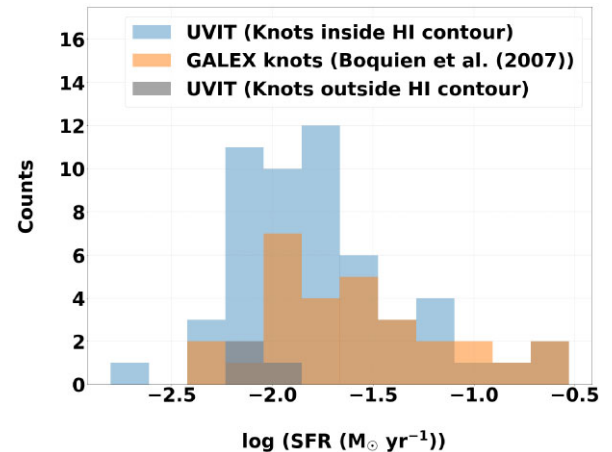


Figure 12. Histograms of SFRs (corrected for extinction) of the knots in this study and SFRs of knots given in Boquien et al. (2007) for the NGC 5291 interacting system.

the three known TDGs in the NGC 5291 system are  $-0.52$  (NGC 5291N),  $-0.52$  (NGC 5291S), and  $-0.66$  (NGC 5291SW).

## 6 SUMMARY

The star forming knots in the NGC 5291 interacting system, which includes three bona fide TDGs and several TDG candidates was investigated using high-resolution FUV and NUV data from AstroSat’s UVIT. The star-formation activity in the selected star-forming knots was further studied by determining their extinction-corrected SFR values. The results are summarized as below:

- (i) A total of 57 star-forming knots have been identified as being part of the NGC 5291 interacting system.
- (ii) The resolved star-forming knots range in size from 1.4 to 11.4 kpc.
- (iii) In comparison to the previous UV imaging at lower resolution, we have 12 new detections. The higher resolution of UVIT has allowed for better de-blending of the structures. Several of the knots

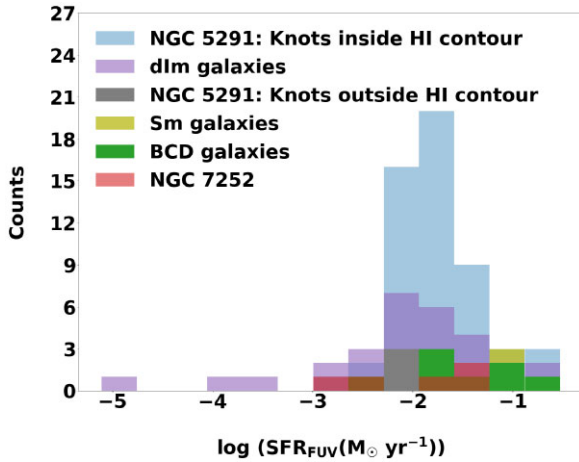


**Figure 13.** Histograms showing the SFR values of the selected knots of the NGC 5291 system as per this study, SFRs of BCD (8 samples), Sm (7 samples), and dIm (29 samples) galaxies in the nearby universe from Hunter et al. (2010) and uncorrected SFR of knots of the NGC 7252 system given in George et al. (2018).

in the NGC 5291 system which appeared as single star forming regions in *GALEX* images are well resolved into smaller star forming knots in the UVIT images.

(iv) The extinction towards each of the resolved star-forming knots and the main body of the NGC 5291 interacting system was computed using the slope of the UV continuum and hence the extinction-corrected SFR was determined. The total extinction-corrected SFR of the knots (inside and outside H I contour), excluding NGC 5291 and Seashell galaxies, is estimated as  $1.75 \pm 0.04 M_{\odot} \text{ yr}^{-1}$ .

(v) Comparison of the NGC 5291 system with NGC 7252 using UVIT data showed that the SFR for both the systems are similar. Also the comparison with independent dwarf galaxy populations (BCD, Sm, and dIm galaxies) in the nearby Universe showed that many of the knots in the NGC 5291 system have SFR values comparable to the SFR of BCD galaxies.

## ACKNOWLEDGEMENTS

The authors RR and GS acknowledge the financial support of ISRO under AstroSat archival Data utilization program (No. DS\_2B-13013(2)/9/2020-Sec.2). This publication uses data from the AstroSat mission of the Indian Space Research Organisation (ISRO), archived at the Indian Space Science Data Centre (ISSDC). RR acknowledges visiting associateship of IUCAA, Pune. KG and LC acknowledge support from the Australia-India Council/Department of Foreign Affairs and Trade (via grant AIC2018-067). We thank Aaron Robotham for help with ProFound. SS acknowledges support from the Science and Engineering Research Board of India through Ramanujan Fellowship and POWER grant (SPG/2021/002672). LC acknowledges support from the Australian Research Council Discovery Project and Future Fellowship funding schemes (DP210100337, FT180100066). This work used ASTROPY, MATPLOTLIB, and REPROJECT software packages (Hunter 2007; Astropy Collaboration 2013, 2018; Robitaille 2018; Astropy Collaboration 2022).

## DATA AVAILABILITY

The Astrosat UVIT imaging data underlying this article are available in ISSDC Astrobrowse archive ([https://astrobrowse.issdc.gov.in/astro\\_archive/archive/Home.jsp](https://astrobrowse.issdc.gov.in/astro_archive/archive/Home.jsp)) and can be accessed with proposal ID: G07\_003.

## REFERENCES

- Alonso-Herrero A., Rieke G. H., Rieke M. J., Scoville N. Z., 2000, *ApJ*, 532, 845
- Astropy Collaboration 2013, *A&A*, 558, A33
- Astropy Collaboration 2018, *AJ*, 156, 123
- Astropy Collaboration 2022, *ApJ*, 935, 167
- Bixler J., Bowyer S., Deharveng J. M., Courtes G., Malina R., Martin C., Lampton M., 1984, *Science*, 225, 184
- Boquien M., Duc P. A., Braine J., Brinks E., Lisenfeld U., Charmandaris V., 2007, *A&A*, 467, 93
- Boquien M. et al., 2009, *AJ*, 137, 4561
- Boquien M. et al., 2012, *A&A*, 539, A145
- Bournaud F., 2010, *Adv. Astron.*, 2010, 1
- Bournaud F. et al., 2007, *Science*, 316, 1166
- Buat V. et al., 2005, *ApJ*, 619, L51
- Buta R., Crocker D. A., 1993, *AJ*, 106, 939
- Calzetti D., Kinney A. L., Storchi-Bergmann T., 1994, *ApJ*, 429, 582
- Conselice C. J., Bershadly M. A., Dickinson M., Papovich C., 2003, *AJ*, 126, 1183
- Cortese L., Gavazzi G., Boselli A., 2008, *MNRAS*, 390, 1282
- Deharveng J. M., Sasseen T. P., Buat V., Bowyer S., Lampton M., Wu X., 1994, *A&A*, 289, 715
- Dey A. et al., 2019, *AJ*, 157, 168
- Duc P.-A., 2012, in Papaderos P., Recchi S., Hensler G., eds, Dwarf Galaxies: Keys to Galaxy Formation and Evolution. Springer, Berlin, p. 305
- Duc P. A., Mirabel I. F., 1998, *A&A*, 333, 813
- Duc P. A., Mirabel I. F., 1999, in Barnes J. E., Sanders D. B., eds, Galaxy Interactions at Low and High Redshift, Vol. 186. Springer, Berlin, p. 61
- Duc P. A., Brinks E., Springel V., Pichardo B., Weilbacher P., Mirabel I. F., 2000, *AJ*, 120, 1238
- Duc P. A., Bournaud F., Masset F., 2004, *A&A*, 427, 803
- Elmegreen B. G., Kaufman M., Thomasson M., 1993, *ApJ*, 412, 90
- Elmegreen B. G. et al., 2020, *ApJ*, 888, L27
- Fensch J. et al., 2019, *A&A*, 628, A60
- George K. et al., 2018, *A&A*, 614, A130
- Gordon K. D., Clayton G. C., Witt A. N., Misselt K. A., 2000, *ApJ*, 533, 236
- Hancock M., Smith B. J., Struck C., Giroux M. L., Hurlock S., 2009, *AJ*, 137, 4643
- Hibbard J. E. et al., 2005, *ApJ*, 619, L87
- Higdon J. L., 1995, *ApJ*, 455, 524
- Higdon S. J., Higdon J. L., Marshall J., 2006, *ApJ*, 640, 768
- Hunter J. D., 2007, *Comput. Sci. Eng.*, 9, 90
- Hunter D. A., Hunsberger S. D., Roye E. W., 2000, *ApJ*, 542, 137
- Hunter D. A., Elmegreen B. G., Ludka B. C., 2010, *AJ*, 139, 447
- Iglesias-Páramo J. et al., 2006, *ApJS*, 164, 38
- Joye W. A., Mandel E., 2003, in Payne H. E., Jedrzejewski R. I., Hook R. N., eds, ASP Conf. Ser. Vol. 295, Astronomical Data Analysis Software and Systems XII. Astron. Soc. Pac., San Francisco, p. 489
- Kennicutt R. C., Evans N. J., 2012, *ARA&A*, 50, 531
- Kumar A. et al., 2012, in Takahashi T., Murray S. S., den Herder J.-W. A., eds, Proc. SPIE Conf. Ser. Vol. 8443, Space Telescopes and Instrumentation 2012: Ultraviolet to Gamma Ray. SPIE, Bellingham, p. 84431N
- Longmore A. J., Hawarden T. G., Cannon R. D., Allen D. A., Mebold U., Goss W. M., Reif K., 1979, *MNRAS*, 188, 285
- Malphrus B. K., Simpson C. E., Gottesman S. T., Hawarden T. G., 1997, *AJ*, 114, 1427
- Meurer G. R., Heckman T. M., Calzetti D., 1999, *ApJ*, 521, 64
- Mirabel I. F., Dottori H., Lutz D., 1992, *A&A*, 256, L19
- Morrissey P. et al., 2007, *ApJS*, 173, 682
- Neff S. G. et al., 2005, *ApJ*, 619, L91
- Okazaki T., Taniguchi Y., 2000, *ApJ*, 543, 149
- Oke J. B., Gunn J. E., 1983, *ApJ*, 266, 713
- Overzier R. A. et al., 2011, *ApJ*, 726, L7
- Pearson W. J. et al., 2019, *A&A*, 631, A51
- Pedersen H., Gammelgaard P., Laustsen S., 1978, *The Messenger*, 13, 11
- Postma J. E., Leahy D., 2017, *PASP*, 129, 115002
- Postma J. E., Leahy D., 2020, *PASP*, 132, 054503

- Postma J. E., Leahy D., 2021, *J. Astrophys. Astron.*, 42, 30  
Robitaille T., 2018, *Reproject: astronomical image reprojection in Python*.  
Available at: <https://doi.org/10.5281/zenodo.1162674>  
Robotham A. S. G., Davies L. J. M., Driver S. P., Koushan S., Taranu D. S.,  
Casura S., Liske J., 2018, *MNRAS*, 476, 3137  
Salpeter E. E., 1955, *ApJ*, 121, 161  
Sheen Y.-K. et al., 2009, *AJ*, 138, 1911  
Sotnikova N. Y., Reshetnikov V. P., 1998, *Astron. Lett.*, 24, 73  
Struck C., 1999, *Phys. Rep.*, 321, 1  
Tandon S. N. et al., 2017, *AJ*, 154, 128  
Tandon S. N. et al., 2020, *AJ*, 159, 158  
Trewhella M., 1998, *MNRAS*, 297, 807  
White S. D. M., Frenk C. S., 1991, *ApJ*, 379, 52  
White S. D. M., Rees M. J., 1978, *MNRAS*, 183, 341

#### APPENDIX: PROPERTIES OF KNOTS IN NGC 5291 INTERACTING SYSTEM

**Table A1.**

Region No.	RA (Degrees)	DEC (Degrees)	Area (arcsec <sup>2</sup> )	Flux (FUV) (ergs cm <sup>-2</sup> s <sup>-1</sup> ) Å <sup>-1</sup>	Flux err (FUV) (ergs cm <sup>-2</sup> s <sup>-1</sup> ) Å <sup>-1</sup>	Flux (NUV) (ergs cm <sup>-2</sup> s <sup>-1</sup> ) Å <sup>-1</sup>	Flux err (NUV) (ergs cm <sup>-2</sup> s <sup>-1</sup> ) Å <sup>-1</sup>	SFR <sub>uncorr</sub> (FUV) (M <sub>⊙</sub> yr <sup>-1</sup> )	SFR <sub>uncorr</sub> err (FUV) (M <sub>⊙</sub> yr <sup>-1</sup> )	β	β err	SFR <sub>corr</sub> (FUV) (M <sub>⊙</sub> yr <sup>-1</sup> )	SFR <sub>corr</sub> err (FUV) (M <sub>⊙</sub> yr <sup>-1</sup> )
<b>Knots inside the H I contour</b>													
1	206.7495	-30.4242	77.4	1.07E-16	6.32E-18	3.66E-17	1.00E-18	5.86E-03	3.48E-04	-2.18	0.13	6.34E-03	1.61E-03
2	206.7513	-30.4195	118.9	1.28E-16	6.92E-18	4.69E-17	1.14E-18	7.02E-03	3.80E-04	-2.04	0.12	9.83E-03	2.27E-03
3	206.7523	-30.4221	107.3	4.00E-16	1.22E-17	1.50E-16	2.03E-18	2.20E-02	6.73E-04	-2.00	0.07	3.34E-02	4.46E-03
4	206.7543	-30.4238	151.3	1.95E-16	8.56E-18	7.01E-17	1.39E-18	1.07E-02	4.70E-04	-2.09	0.10	1.38E-02	2.60E-03
5	206.7647	-30.3707	127.2	7.11E-16	1.63E-17	2.64E-16	2.70E-18	3.91E-02	8.97E-04	-2.02	0.05	5.73E-02	5.90E-03
6	206.7928	-30.4638	76.5	1.61E-16	7.76E-18	6.22E-17	1.31E-18	8.84E-03	4.27E-04	-1.93	0.11	1.51E-02	3.10E-03
7	206.8064	-30.3829	84.2	1.09E-16	6.40E-18	4.09E-17	1.06E-18	6.00E-03	3.52E-04	-2.00	0.13	9.03E-03	2.25E-03
8	206.8194	-30.4738	157.8	3.39E-16	1.13E-17	1.22E-16	1.83E-18	1.86E-02	6.19E-04	-2.08	0.08	2.43E-02	3.51E-03
9	206.8217	-30.3431	58.0	1.90E-16	8.44E-18	7.66E-17	1.45E-18	1.04E-02	4.64E-04	-1.85	0.10	2.07E-02	3.92E-03
10	206.8228	-30.4483	73.9	1.05E-16	6.28E-18	3.65E-17	1.00E-18	5.79E-03	3.45E-04	-2.16	0.14	6.55E-03	1.67E-03
11	206.8234	-30.4719	211.6	2.78E-15	3.23E-17	9.98E-16	5.24E-18	1.53E-01	1.77E-03	-2.09	0.03	1.97E-01	1.19E-02
12	206.8236	-30.3338	149.6	3.24E-16	1.10E-17	1.37E-16	1.94E-18	1.78E-02	6.06E-04	-1.76	0.08	4.22E-02	6.17E-03
13	206.8237	-30.3379	28.8	6.31E-17	4.87E-18	2.58E-17	8.42E-19	3.47E-03	2.67E-04	-1.83	0.17	7.22E-03	2.34E-03
14	206.8243	-30.4426	79.1	1.21E-16	6.74E-18	4.52E-17	1.11E-18	6.66E-03	3.71E-04	-2.01	0.12	9.91E-03	2.35E-03
15	206.8245	-30.3662	120.3	1.86E-16	8.34E-18	7.73E-17	1.46E-18	1.02E-02	4.58E-04	-1.79	0.10	2.28E-02	4.36E-03
16	206.8252	-30.3528	108.0	4.61E-16	1.31E-17	1.81E-16	2.23E-18	2.53E-02	7.23E-04	-1.91	0.07	4.53E-02	5.65E-03
17	206.8252	-30.3428	85.2	1.88E-16	8.39E-18	7.01E-17	1.39E-18	1.03E-02	4.61E-04	-2.01	0.10	1.54E-02	2.95E-03
18	206.8255	-30.3642	80.9	2.06E-16	8.79E-18	8.21E-17	1.50E-18	1.13E-02	4.83E-04	-1.88	0.10	2.14E-02	3.90E-03
19	206.8259	-30.3583	100.0	1.34E-16	7.09E-18	5.49E-17	1.23E-18	7.37E-03	3.90E-04	-1.82	0.12	1.55E-02	3.46E-03
20	206.8271	-30.3440	84.0	2.03E-16	8.73E-18	8.70E-17	1.55E-18	1.12E-02	4.80E-04	-1.73	0.10	2.78E-02	5.07E-03
21	206.8276	-30.3544	59.4	1.49E-16	7.48E-18	5.69E-17	1.25E-18	8.21E-03	4.11E-04	-1.97	0.11	1.32E-02	2.82E-03
22	206.8276	-30.3571	43.4	7.96E-17	5.46E-18	3.21E-17	9.39E-19	4.37E-03	3.00E-04	-1.85	0.15	8.71E-03	2.52E-03
23	206.8315	-30.4441	165.4	5.32E-16	1.41E-17	2.18E-16	2.45E-18	2.92E-02	7.76E-04	-1.82	0.06	6.12E-02	7.13E-03
24	206.8329	-30.3398	267.4	6.13E-16	1.52E-17	2.42E-16	2.58E-18	3.37E-02	8.33E-04	-1.89	0.06	6.21E-02	6.79E-03
25	206.8355	-30.4565	150.1	1.66E-16	7.88E-18	6.15E-17	1.30E-18	9.10E-03	4.33E-04	-2.02	0.11	1.32E-02	2.70E-03
26	206.8355	-30.3479	368.1	2.59E-15	3.12E-17	1.06E-15	5.39E-18	1.42E-01	1.71E-03	-1.82	0.03	2.97E-01	1.82E-02
27	206.8366	-30.4458	178.1	2.68E-16	1.00E-17	9.43E-17	1.61E-18	1.48E-02	5.51E-04	-2.13	0.09	1.75E-02	2.84E-03
28	206.8370	-30.3589	77.8	1.40E-16	7.25E-18	5.38E-17	1.22E-18	7.72E-03	3.99E-04	-1.96	0.12	1.26E-02	2.78E-03
29	206.8383	-30.3397	65.8	1.06E-16	6.30E-18	3.97E-17	1.04E-18	5.81E-03	3.46E-04	-2.00	0.13	8.82E-03	2.23E-03
30	206.8386	-30.3574	66.3	8.77E-17	5.73E-18	3.22E-17	9.41E-19	4.82E-03	3.15E-04	-2.04	0.15	6.78E-03	1.88E-03
31	206.8388	-30.3506	102.7	1.37E-16	7.17E-18	5.43E-17	1.22E-18	7.54E-03	3.94E-04	-1.89	0.12	1.40E-02	3.10E-03
32	206.8408	-30.3450	85.6	1.70E-16	7.98E-18	6.70E-17	1.36E-18	9.32E-03	4.38E-04	-1.89	0.11	1.71E-02	3.43E-03
33	206.8425	-30.3830	50.7	7.61E-17	5.34E-18	2.87E-17	8.87E-19	4.18E-03	2.94E-04	-1.99	0.16	6.43E-03	1.91E-03
34	206.8433	-30.3493	58.0	7.27E-17	5.22E-18	2.52E-17	8.33E-19	4.00E-03	2.87E-04	-2.16	0.17	4.54E-03	1.39E-03
35	206.8440	-30.3698	54.7	7.92E-17	5.45E-18	2.74E-17	8.68E-19	4.35E-03	3.00E-04	-2.16	0.16	4.90E-03	1.44E-03
36	206.8450	-30.4353	86.1	8.52E-17	5.65E-18	3.58E-17	9.91E-19	4.68E-03	3.11E-04	-1.77	0.15	1.08E-02	3.02E-03
37	206.8454	-30.4647	387.0	1.25E-15	2.17E-17	4.66E-16	3.58E-18	6.89E-02	1.19E-03	-2.02	0.04	1.01E-01	8.14E-03
38	206.8457	-30.3640	34.4	4.95E-17	4.31E-18	2.01E-17	7.44E-19	2.72E-03	2.37E-04	-1.83	0.19	5.60E-03	2.05E-03
39	206.8459	-30.4583	212.4	1.55E-15	2.41E-17	6.29E-16	4.16E-18	8.52E-02	1.32E-03	-1.84	0.04	1.74E-01	1.28E-02
40	206.8462	-30.4619	12.5	2.54E-17	3.08E-18	8.80E-18	4.92E-19	1.39E-03	1.69E-04	-2.16	0.27	1.58E-03	8.15E-04
41	206.8477	-30.4558	77.1	9.90E-17	6.09E-18	3.78E-17	1.02E-18	5.44E-03	3.35E-04	-1.96	0.14	8.85E-03	2.31E-03
42	206.8479	-30.4496	82.6	2.29E-16	9.27E-18	8.23E-17	1.50E-18	1.26E-02	5.10E-04	-2.09	0.09	1.62E-02	2.82E-03

Table A1 – continued

Region No.	RA (Degrees)	DEC (Degrees)	Area (arcsec <sup>2</sup> )	Flux (FUV) (ergs cm <sup>-2</sup> s <sup>-1</sup> Å <sup>-1</sup> )	Flux err (FUV) (ergs cm <sup>-2</sup> s <sup>-1</sup> Å <sup>-1</sup> )	Flux (NUV) (ergs cm <sup>-2</sup> s <sup>-1</sup> Å <sup>-1</sup> )	Flux err (NUV) (ergs cm <sup>-2</sup> s <sup>-1</sup> Å <sup>-1</sup> )	SFR <sub>uncorr</sub> (FUV) (M <sub>⊙</sub> yr <sup>-1</sup> )	SFR <sub>uncorr</sub> err (FUV) (M <sub>⊙</sub> yr <sup>-1</sup> )	β	β err	SFR <sub>corr</sub> (FUV) (M <sub>⊙</sub> yr <sup>-1</sup> )	SFR <sub>corr</sub> err (FUV) (M <sub>⊙</sub> yr <sup>-1</sup> )
43	206.8482	-30.4475	44.8	1.87E-16	8.36E-18	7.01E-17	1.39E-18	1.03E-02	4.60E-04	-1.99	0.10	1.57E-02	3.01E-03
44	206.8488	-30.4452	156.2	2.85E-16	1.03E-17	1.10E-16	1.74E-18	1.56E-02	5.68E-04	-1.94	0.08	2.65E-02	4.14E-03
45	206.8489	-30.4625	64.0	1.71E-16	8.00E-18	6.65E-17	1.35E-18	9.38E-03	4.40E-04	-1.92	0.11	1.64E-02	3.27E-03
46	206.8493	-30.4521	171.3	5.25E-16	1.40E-17	2.06E-16	2.38E-18	2.88E-02	7.71E-04	-1.91	0.06	5.19E-02	6.09E-03
47	206.8501	-30.4391	101.4	2.70E-16	1.01E-17	1.09E-16	1.73E-18	1.48E-02	5.53E-04	-1.84	0.08	3.01E-02	4.80E-03
48	206.8509	-30.4322	42.9	8.61E-17	5.68E-18	3.65E-17	1.00E-18	4.73E-03	3.12E-04	-1.75	0.15	1.14E-02	3.16E-03
49	206.8514	-30.4342	48.6	7.78E-17	5.40E-18	3.04E-17	9.14E-19	4.27E-03	2.97E-04	-1.91	0.16	7.58E-03	2.22E-03
50	206.8518	-30.4430	146.5	1.96E-16	8.56E-18	7.75E-17	1.46E-18	1.07E-02	4.71E-04	-1.89	0.10	2.00E-02	3.73E-03
51	206.8576	-30.4298	65.6	1.22E-16	6.77E-18	4.78E-17	1.15E-18	6.73E-03	3.72E-04	-1.92	0.23	1.19E-02	2.78E-03
52	206.8583	-30.4277	61.8	1.23E-16	6.80E-18	5.04E-17	1.18E-18	6.77E-03	3.74E-04	-1.82	0.12	1.41E-02	3.30E-03
53	206.8606	-30.4306	171.6	5.45E-16	1.43E-17	2.02E-16	2.35E-18	2.99E-02	7.85E-04	-2.03	0.06	4.31E-02	5.00E-03
54	206.8663	-30.4148	49.5	7.02E-17	5.13E-18	2.83E-17	8.82E-19	3.86E-03	2.82E-04	-1.85	0.16	7.69E-03	2.37E-03
<b>Knots outside the H I contour</b>													
55	206.7629	-30.4293	109.2	1.11E-16	6.46E-18	3.88E-17	1.03E-18	6.12E-03	3.55E-04	-2.15	0.13	7.05E-03	1.75E-03
56	206.7918	-30.3138	59.4	8.80E-17	5.74E-18	3.63E-17	9.99E-19	4.83E-03	3.16E-04	-1.80	0.15	1.05E-02	2.89E-03
57	206.8662	-30.4428	119.9	1.41E-16	7.27E-18	4.79E-17	1.15E-18	7.74E-03	3.99E-04	-2.20	0.12	8.12E-03	1.80E-03
<b>NGC 5291</b>	206.8502	-30.4107	30.9	4.91E-17	4.29E-18	2.85E-17	8.85E-19	2.70E-03	2.36E-04	-1.11	0.19	2.09E-02	7.50E-03
	206.8513	-30.4039	30.7	5.49E-17	4.54E-18	3.80E-17	1.02E-18	3.02E-03	2.49E-04	-0.751	0.178	4.51E-02	1.52E-02
	206.8547	-30.4066	64.6	9.77E-17	6.05E-18	7.12E-17	1.40E-18	5.37E-03	3.33E-04	-0.645	0.134	9.75E-02	2.47E-02
	206.8515	-30.4063	224.2	5.01E-16	1.37E-17	5.12E-16	3.75E-18	2.75E-02	7.53E-04	0.046	0.061	1.77E+00	2.03E-01
<b>Seashell</b>	206.8493	-30.4164	11.8	2.85E-17	3.27E-18	2.25E-17	7.87E-19	1.57E-03	1.80E-04	-0.479	0.245	3.85E-02	1.79E-02
	206.8503	-30.4159	31.1	5.82E-17	4.67E-18	5.28E-17	1.20E-18	3.20E-03	2.57E-04	-0.200	0.171	1.31E-01	4.25E-02
	206.8471	-30.4175	159.8	2.68E-16	1.00E-17	2.78E-16	2.76E-18	1.47E-02	5.51E-04	0.071	0.081	9.93E-01	1.52E-01
<b>Possible contaminant knots inside H I contour</b>													
58	206.8128	-30.3607	34.4	7.37E-17	5.26E-18	3.14E-17	9.29E-19	4.05E-03	2.89E-04	-1.74	0.16	9.89E-03	2.96E-03
59	206.8226	-30.3391	76.4	1.74E-16	8.09E-18	8.08E-17	1.49E-18	9.58E-03	4.44E-04	-1.57	0.10	3.21E-02	6.26E-03
60	206.8261	-30.3555	29.0	6.90E-17	5.09E-18	3.30E-17	9.52E-19	3.79E-03	2.80E-04	-1.50	0.16	1.43E-02	4.38E-03
61	206.8326	-30.4458	52.4	1.20E-16	6.71E-18	5.23E-17	1.20E-18	6.60E-03	3.69E-04	-1.70	0.13	1.74E-02	4.10E-03
62	206.8389	-30.4723	193.2	3.31E-16	1.11E-17	1.78E-16	2.21E-18	1.82E-02	6.12E-04	-1.27	0.08	1.05E-01	1.50E-02
63	206.8416	-30.4005	64.2	8.82E-17	5.75E-18	3.77E-17	1.02E-18	4.85E-03	3.16E-04	-1.73	0.15	1.20E-02	3.28E-03
64	206.8424	-30.4637	14.8	3.24E-17	3.49E-18	1.56E-17	6.54E-19	1.78E-03	1.92E-04	-1.49	0.24	6.81E-03	3.04E-03
65	206.8435	-30.3625	204.8	3.63E-16	1.17E-17	1.58E-16	2.08E-18	2.00E-02	6.41E-04	-1.69	0.07	5.29E-02	7.32E-03
66	206.8499	-30.4650	67.5	8.31E-17	5.58E-18	3.55E-17	9.88E-19	4.56E-03	3.07E-04	-1.73	0.15	1.13E-02	3.18E-03
67	206.8568	-30.4234	26.2	5.23E-17	4.43E-18	2.34E-17	8.01E-19	2.87E-03	2.43E-04	-1.64	0.09	8.39E-03	2.97E-03
<b>Possible contaminant knots outside the H I contour</b>													
68	206.7684	-30.4745	24.3	3.83E-17	3.76E-18	1.76E-17	6.95E-19	2.10E-03	2.08E-04	-1.59	0.22	6.79E-03	2.80E-03
69	206.8093	-30.3437	58.5	6.64E-17	4.99E-18	2.98E-17	9.05E-19	3.65E-03	2.74E-04	-1.63	0.17	1.08E-02	3.40E-03
70	206.8373	-30.4912	34.4	7.14E-17	5.17E-18	3.86E-17	1.03E-18	3.92E-03	2.84E-04	-1.25	0.16	2.34E-02	7.01E-03
71	206.8715	-30.4765	48.2	1.32E-16	7.05E-18	8.91E-17	1.56E-18	7.28E-03	3.87E-04	-0.81	0.12	9.79E-02	2.14E-02
72	206.8788	-30.3255	62.0	1.00E-16	6.13E-18	4.97E-17	1.17E-18	5.50E-03	3.37E-04	-1.43	0.14	2.38E-02	6.08E-03
73	206.8861	-30.4796	59.9	8.77E-17	5.73E-18	5.36E-17	1.21E-18	4.82E-03	3.15E-04	-1.00	0.14	4.53E-02	1.22E-02
74	206.8892	-30.4857	112.8	1.29E-16	6.96E-18	6.37E-17	1.32E-18	7.11E-03	3.83E-04	-1.44	0.12	2.98E-02	6.70E-03

 This paper has been typeset from a L<sup>A</sup>T<sub>E</sub>X file prepared by the author.